

Assessment of a bidirectional reflectance distribution correction of above-water and satellite water-leaving radiance in coastal waters

Soe Hlaing,¹ Alexander Gilerson,^{1,*} Tristan Harmel,¹ Alberto Tonizzo,¹
Alan Weidemann,² Robert Arnone,² and Samir Ahmed¹

¹Optical Remote Sensing Laboratory, The City College of the City University of New York, New York 10031, USA

²Naval Research Laboratory, Stennis Space Center, Mississippi 39529, USA

*Corresponding author: gilerson@ccny.cuny.edu

Received 1 August 2011; revised 19 October 2011; accepted 23 October 2011;
posted 31 October 2011 (Doc. ID 152078); published 9 January 2012

Water-leaving radiances, retrieved from *in situ* or satellite measurements, need to be corrected for the bidirectional properties of the measured light in order to standardize the data and make them comparable with each other. The current operational algorithm for the correction of bidirectional effects from the satellite ocean color data is optimized for typical oceanic waters. However, versions of bidirectional reflectance correction algorithms specifically tuned for typical coastal waters and other case 2 conditions are particularly needed to improve the overall quality of those data. In order to analyze the bidirectional reflectance distribution function (BRDF) of case 2 waters, a dataset of typical remote sensing reflectances was generated through radiative transfer simulations for a large range of viewing and illumination geometries. Based on this simulated dataset, a case 2 water focused remote sensing reflectance model is proposed to correct above-water and satellite water-leaving radiance data for bidirectional effects. The proposed model is first validated with a one year time series of *in situ* above-water measurements acquired by collocated multispectral and hyperspectral radiometers, which have different viewing geometries installed at the Long Island Sound Coastal Observatory (LISCO). Match-ups and intercomparisons performed on these concurrent measurements show that the proposed algorithm outperforms the algorithm currently in use at all wavelengths, with average improvement of 2.4% over the spectral range. LISCO's time series data have also been used to evaluate improvements in match-up comparisons of Moderate Resolution Imaging Spectroradiometer satellite data when the proposed BRDF correction is used in lieu of the current algorithm. It is shown that the discrepancies between coincident *in-situ* sea-based and satellite data decreased by 3.15% with the use of the proposed algorithm. This confirms the advantages of the proposed model over the current one, demonstrating the need for a specific case 2 water BRDF correction algorithm as well as the feasibility of enhancing performance of current and future satellite ocean color remote sensing missions for monitoring of typical coastal waters.

1. Introduction

The water-leaving radiance field emerging from sea water is not generally isotropic because of the nonisotropic character of the volume scattering function (VSF) of the water body, coupled with nonisotropic illumination conditions that generally prevail above the sea surface. Furthermore, the wavy nature of the

water surface also has noticeable influence over the anisotropy of the water-leaving radiance field. The bidirectional structure of the emerging radiance field has implications, particularly in the processing of data from ocean color satellite sensors as well as in calibration/validation activities for ocean color sensors in which water-leaving radiances obtained under various geometrical configurations have to be quantitatively and accurately compared.

Variations in the bidirectional properties of the upward radiative field have already been extensively

1559-128X/12/020220-18\$15.00/0
© 2012 Optical Society of America

studied. Morel and Gentili [1] reported the variations in the bidirectional properties of the upward radiative field for case 1 waters, and their studies related the bidirectional variations of the water-leaving radiance field to chlorophyll concentration, [Chl]. Their findings were also corroborated by field measurements obtained using an underwater radiance distribution camera system in low-chlorophyll case 1 waters [2]. The anisotropy of the water-leaving radiance was also discerned from the series of BRDF measurements carried out from research aircraft for both case 1 and case 2 waters [3]. These airborne measurement results show good overall agreement with theoretical simulations. Also based on the field measurements performed exclusively for case 1 water types, Voss and Morel reported that the Q factor, defined as the ratio between upwelling irradiance and upwelling radiance from the sea surface, can vary within 7% [4]. These predictive investigations were tentatively extended to typical case 2 waters, usually dominated by sediment or by colored dissolved organic matter (CDOM), and are currently being used in the NASA ocean color data processing procedures as the operational correction algorithm [5] for the retrieval of water-leaving radiance from both case 1 and case 2 water types. Although the current operational algorithm is considered reasonably effective for case 1 water conditions, the validity of this correction algorithm in case 2 water types has not been really verified in natural environments [6]. Accordingly, the need for an improved version of a bidirectional reflectance correction algorithm particularly tuned for typical case 2 water conditions is the general consensus among the ocean color radiometry community [6,7].

In case 2 waters, the more complex variability of the water composition results in the bidirectional properties of the upwelling radiance field being severely affected by concentrations of CDOM and mineral particles, which can have significant consequences on the correction factors both spectrally and angularly [7]. Consequently, extensive studies of the bidirectional properties of case 2 waters have been made through radiative transfer simulations with inputs of inherent optical properties (IOPs) typical for case 2 water types. Lee *et al.* proposed a semianalytical model that relates nadir viewing remote sensing reflectance to single backscattering albedo and the solar zenith angle for both deep and shallow waters [8,9]. This model was later extended as both viewing and solar zenith angle dependent to be used for measurements made at various viewing angles [9]. Parameterization of the remote sensing reflectance as a function of single backscattering albedo, solar zenith and sensor viewing angles, and the sea surface wind speed was also developed by Albert and Mobley [10] and Albert and Gege [11]. Nevertheless, these models do not take into account the solar-sensor relative azimuth angle as an input parameter, and as a result, bidirectional variations in the azimuthal direction cannot be analyzed with the use of these models.

Notably, Park and Ruddick [6] proposed a remote sensing reflectance model based on lookup tables of coefficients generated for a large range of solar zenith, sensor viewing, and solar-sensor relative azimuth angles to estimate the directional variation of the water-leaving radiance field of both case 1 and case 2 waters. However, their model requires a phase function parameter defined by the contribution of suspended particles to the backscattering coefficients. But in remote sensing of coastal waters, accurate retrieval of such parameters of the water body remains highly challenging, and this can limit the operational use of the algorithm. Lee *et al.* [12] also proposed an approach centered on the IOP of water to remove the angular variations in remote sensing reflectance measurements. The evaluations of the overall performance of their BRDF correction scheme carried out with the use of the field measured data indicate slight improvement over the current standard correction algorithm.

In our previous studies [7], bidirectional reflectance effects of coastal waters were analyzed through extensive radiative transfer simulations of remote sensing reflectances typical for a wide range of coastal water conditions. Based on this analysis, we proposed a model that relates the single backscattering albedo to the remote sensing reflectance through a least mean squared optimization for a large range of IOPs and of viewing and illumination geometries. Furthermore, the bidirectional reflectance parameter Q was also analyzed based on a microphysical model of the water constituents and was observed to have variations with a wavelength of about 15%, especially in the blue and green regions of the water-leaving radiance spectrum, depending on the water composition.

As an extension of the previous model, we propose, in this paper, an improved version of the remote sensing reflectance model based on lookup tables generated for a large set of illumination and viewing geometries and water optical properties, to estimate the directional variation of the water-leaving radiance field of typical case 2 water conditions. Unlike previous studies [6,7,12], the model coefficients were generated as being wavelength dependent in order to better deal with the spectral dependency of bidirectional effects. The proposed model is applied to two different above-water datasets acquired by collocated instruments on the Long Island Sound Coastal Observatory (LISCO). The LISCO site, near Northport, New York, has been established to support present and future multispectral and hyperspectral ocean color sensor calibration/validation activities, as well as the development of new measurement and retrieval techniques and algorithms for coastal waters [13–15]. These sea-based datasets also permit us to examine and validate satellite retrievals based on the proposed and the current BRDF algorithms.

In Section 2, fundamental equations and rationale of remote sensing reflectance retrieval are briefly revisited. The following section, Section 3, deals with

the radiative transfer modeling of coastal waters and the details of the proposed BRDF correction scheme. Theoretical and noise sensitivity analysis based on the simulated dataset is described in Section 4. The performances of the new scheme are tested in Section 5 based on time series of coincident remote sensing reflectance measurements at different scattering angles from the LISCO platform. Finally, the proposed BRDF correction scheme is applied to Moderate Resolution Imaging Spectroradiometer (MODIS) satellite data, and its performance is discussed based on comparisons with the sea-based LISCO datasets. This is followed by concluding remarks.

2. Theoretical Background

The fundamental equation, shown below, relates any slanted radiance exiting the water, L_w , to the downwelling irradiance just above the sea surface, E_d , and to the absorption and backscattering coefficients of the water body (a and b_b) through three quantities: \mathfrak{R} (a dimensionless factor that merges all the reflection and refraction effects that occur when downward irradiance and upward radiance propagate through the air–water interface), f (a dimensionless coefficient that relates the magnitude of the irradiance reflectance just below the surface to the IOPs, namely a and b_b) and Q (the bidirectional function with units of sr^{-1}) as follows [5]:

$$L_w(\theta_s, \theta_v, \phi, \lambda, W, \text{IOP}) = E_d(\theta_s, \lambda) \times \mathfrak{R}(\theta_s, \theta_v, \lambda, W) \times \frac{f(\theta_s, \lambda, W, \text{IOP})}{Q(\theta_s, \theta_v, \phi, \lambda, W, \text{IOP})} \times \frac{b_b(\lambda)}{a(\lambda) + b_b(\lambda)}. \quad (1)$$

The water-leaving radiance, L_w , at a given wavelength, λ , depends on its own direction, depicted by θ_v , the viewing zenith angle, and ϕ , the relative azimuth angle from the Sun's direction, on the illumination conditions (determined by the solar zenith angle, θ_s), on the sea state (parameterized via the wind speed, W), and on the IOPs of the water body itself. In contrast, besides atmospheric parameters, E_d is only a function of the solar zenith angle, θ_s , and the wavelength. The last factor, $b_b/(a + b_b)$, is customarily called single backscattering albedo, and it is routinely denoted as ω . In Eq. (1) θ_v is the in-water viewing angle, and it is related to θ_v through Snell's law ($\sin \theta_v = n \sin \theta'_v$, where n is the refractive index of water).

The above-water remote sensing reflectance (Rrs) is defined as [16]

$$\text{Rrs}(\theta_s, \theta_v, \phi, \lambda, W, \text{IOP}) = \frac{L_w(\theta_s, \theta_v, \phi, \lambda, W, \text{IOP})}{E_d(\theta_s, \lambda)}. \quad (2)$$

Therefore, from Eqs. (1) and (2), Rrs can be related to \mathfrak{R} , f , Q , and the IOPs of the water as follows:

$$\begin{aligned} \text{Rrs}(\theta_s, \theta_v, \phi, \lambda, W, \text{IOP}) &= \mathfrak{R}(\theta_s, \theta'_v, \lambda, W) \\ &\times \frac{f(\theta_s, \lambda, W, \text{IOP})}{Q(\theta_s, \theta_v, \phi, \lambda, W, \text{IOP})} \\ &\times \omega(\lambda). \end{aligned} \quad (3)$$

On the other hand, Gordon *et al.* [17] showed that nadir viewed remote sensing reflectance can be modeled as the polynomial function of ω . It was also shown in [10,18] that the factor f/Q can be parameterized as the function of ω , θ_s , and θ_v for both deep and shallow waters. In fact, ω can be considered as the representative of the IOP input argument to the f/Q factor, and the relationship between them has to be subsequently expressed in linear or higher order polynomial functions [7,10,18]. Consequently, the relationship between $\text{Rrs}(\lambda)$ and $\omega(\lambda)$ is also considered to be a second or higher degree polynomial [6,7,10,12,17–19]. In this study, we model $\text{Rrs}(\lambda)$ as the third order polynomial of $\omega(\lambda)$ as follows:

$$\text{Rrs}(\theta_s, \theta_v, \phi, \lambda, \omega) = \sum_{i=1}^3 \alpha_i(\theta_s, \theta_v, \phi, \lambda) \omega^i(\lambda), \quad (4)$$

and the model coefficients, α_i , of the relationship [Eq. (4)] are tabulated for a large range of solar zenith (θ_s), viewing (θ_v), and relative azimuth (ϕ) angles as well as for wavelengths (λ). This polynomial model merges all bidirectional effects and directly relates the Rrs to the single parameter ω , allowing the BRDF correction to be performed using only the information on the viewing and illumination geometries at the time of the Rrs measurements. Thus, the model offers a computationally straightforward and simple approach for performing the directional correction by forgoing the potential to model the different influences on L_w (and consequently on the Rrs) separately as in Eqs. (1) and (3).

Based on the simulated dataset, which will be detailed in the following section, it was found that higher order polynomials render less least square (LSQ) curve fitting errors. Nevertheless, it was also observed that higher than third order polynomial fittings also show tendencies to give unrealistic Rrs values if the input ω values were outside the range of the simulated dataset. Thus, we decided to use the third order as the optimal polynomial degree in our modeling. The fundamental difference between the proposed model and the previous models is that, unlike previous studies, model coefficients of the Rrs– ω relationship are generated as wavelength dependent in order to better deal with the known spectral variation in the Q factor [7,18]. Thus, this proposed model allows the BRDF correction to be performed for each wavelength independently, demonstrating the potential for better dealing with the spectral dependency of the BRDF [5,7,18]. In the proposed model, the factor \mathfrak{R} is integrated in the formulation by directly relating ω to the above-water simulated Rrs. Morel *et al.* previously reported large variation in

It with wind speed [5,20]. Nevertheless, Gordon's revision [21] of their results later showed that the influence of surface roughness on the transfer of subsurface radiance through the air–water interface is minimal for surface viewing angles $\theta_v \leq 60^\circ$. Albert and Mobley have also studied the dependence of irradiance reflectance for infinitely deep waters on surface wind, obtaining the same results [10]. Also, Park and Ruddick [6], based on the Hydrolight simulations for IOPs of both case 1 and 2 waters with the different input wind speeds (0, 5 and 10 ms^{-1}), showed the effect of wind speed on bidirectional reflectance to be small. Following these conclusions, we did not incorporate the wind speed (W) as an input parameter, because its influence on both the transfer of subsurface radiance through the air–water interface and the underwater radiance field is minimal [12,21]. It should be noted that the BRDF correction usually accounts for 10%–20% of $R_{rs}(\lambda)$ [6,7]. Thus, the estimation of the correction quality is a challenging task, especially for the field data, where other factors can contribute significantly to total uncertainties.

3. Coastal Waters Radiative Transfer Modeling

3.1. IOP Model

A dataset of remote sensing reflectance spectra, $R_{rs}(\lambda)$, typical for coastal water conditions has been generated by us through radiative transfer simulations using Hydrolight 5 [22]. In these simulations, a four-component bio-optical model was assumed. The four components are pure sea water, CDOM, nonalgal particulates (NAP), and chlorophyll-containing particles (phytoplankton). We use the subscripts “ w ,” “ y ,” “NAP,” and “Chl” to identify these four components in the text below. The input parameters for the modeled IOPs of the components (except for pure sea water) are generated as uniformly distributed random variables in the prescribed ranges typical for coastal water conditions. The most important relationships used to compute the input IOP parameters are detailed in the following paragraphs.

The total spectral absorption coefficient $a(\lambda)$ is given as

$$a(\lambda) = a_w(\lambda) + a_y(\lambda) + a_{\text{Chl}}(\lambda) + a_{\text{NAP}}(\lambda), \quad (5)$$

where the water absorption spectrum $a_w(\lambda)$ was obtained from Pope and Fry [23]. The chlorophyll absorption coefficient for case 2 waters was considered proportional to [Chl] as is often assumed [24] and is given by

$$a_{\text{Chl}}(\lambda) = [\text{Chl}] \cdot a_{\text{Chl}}^*(\lambda), \quad (6)$$

where $a_{\text{Chl}}^*(\lambda)$ is the specific chlorophyll absorption coefficient, in m^2/mg . With a wide variety of specific absorption spectra available, in our simulations the set of specific chlorophyll absorptions was taken from

Ciotti *et al.* [25] as a sum of specific absorptions of microplankton (a_{micro}^*) and picoplankton (a_{pico}^*) with different weighting factors, S_f , as follows:

$$a_{\text{Chl}}^*(\lambda) = S_f \cdot a_{\text{pico}}^*(\lambda) + (1 - S_f) \cdot a_{\text{micro}}^*(\lambda), \quad (7)$$

where $S_f = [0.1, 0.2, 0.3]$. However, a recent study [26] showed that the use of these values generally leads to an underestimation of a_{Chl}^* in the red and near-IR parts of the spectrum. Consequently, we modified the spectra shape in the 650–700 nm part of the spectrum by setting a_{Chl}^* values at 675 nm to 0.0142, 0.0156, and 0.02 m^2/mg for $S_f = 0.1, 0.2,$ and $0.3,$ respectively.

The absorption spectra of NAP and CDOM were both modeled as having exponentially decreasing magnitudes with respect to the wavelength and determined from their base reference values at 400 nm as in [27,28]. A minerogenic particle type is assumed for NAP, and its absorption spectra is modeled as follows:

$$a_{\text{NAP}}(\lambda) = C_{\text{NAP}} \cdot a_{\text{NAP}}^*(400) \cdot \exp(-S_{\text{NAP}}(\lambda - 400)), \quad (8)$$

where $a_{\text{NAP}}^*(400)$ is the specific absorption of NAP at 400 nm in m^2/g , and C_{NAP} is their concentration in g/m^3 . CDOM absorption was also modeled as shown below:

$$a_y(\lambda) = a_y(400) \cdot \exp(-S_y(\lambda - 400)), \quad (9)$$

where $a_y(400)$ is the absorption of CDOM at 400 nm. In Eqs. (8) and (9), S_{NAP} and S_y denote the spectral slopes for the absorption spectra of NAP and CDOM, respectively.

In a similar way, the total scattering coefficient was simulated as a sum of three components:

$$b(\lambda) = b_w(\lambda) + b_{\text{Chl}}(\lambda) + b_{\text{NAP}}(\lambda), \quad (10)$$

where $b(\lambda)$ is the total scattering coefficient in m^{-1} . The scattering of NAP is modeled as a power law function [29] as follows:

$$b_{\text{NAP}}(\lambda) = C_{\text{NAP}} \cdot b_{\text{NAP}}^*(550) \cdot \left(\frac{550}{\lambda}\right)^{\gamma_{\text{NAP}}}, \quad (11)$$

where $b_{\text{NAP}}^*(550)$ is the specific scattering of NAP at 550 nm, in m^2/g .

The scattering coefficient of phytoplankton is calculated as the difference between the attenuation and the absorption coefficients:

$$b_{\text{Chl}}(\lambda) = c_{\text{Chl}}(\lambda) - a_{\text{Chl}}(\lambda), \quad (12)$$

where $b_{\text{Chl}}(\lambda)$ and $c_{\text{Chl}}(\lambda)$ are the scattering and attenuation spectra of phytoplankton. Then the attenuation spectrum is modeled as a power law function [30] as follows:

$$c_{\text{Chl}}(\lambda) = p \cdot [\text{Chl}]^{0.62} \cdot \left(\frac{550}{\lambda}\right)^{\gamma_{\text{chl}}}. \quad (13)$$

The backscattering coefficient can be broken down as the sum of the contributions of the main scattering constituents:

$$b_b(\lambda) = b_{bw}(\lambda) + \bar{b}_{b\text{Chl}} * b_{\text{Chl}}(\lambda) + \bar{b}_{b\text{NAP}} * b_{\text{NAP}}(\lambda), \quad (14)$$

where $b_{bw}(\lambda)$ is obtained in accordance with [31], and $\bar{b}_{b\text{Chl}}$ and $\bar{b}_{b\text{NAP}}$ are the backscattering ratios for chlorophyll and NAP, assumed to be independent of wavelength. $\bar{b}_{b\text{Chl}}$ is calculated according to the following empirical parameterization proposed by Morel *et al.* [5]:

$$\bar{b}_{b\text{Chl}} = 0.002 + \{0.01[0.5 - 0.25 \log_{10}(\text{Chl})]\}. \quad (15)$$

This allows us to use a particle phase function that is able to change progressively with [Chl] value, in such a way that the backscattering efficiency can decrease with increasing [Chl] [5]. $\bar{b}_{b\text{NAP}}$ is taken as a fixed value of 0.0183 assuming a strong mineral component in NAP.

Similar to the procedures followed for total absorption and scattering coefficients, the VSF, denoted as $\beta(\psi)$, is broken down as the sum of the contributions of pure water (β_w), NAP (β_{NAP}), and chlorophyll-containing particles (β_{Chl}) and can be written into the summation of all three components:

$$\beta(\psi) = \beta_w(\psi) + \beta_{\text{NAP}}(\psi) + \beta_{\text{Chl}}(\psi). \quad (16)$$

Equation (16) can be also written in terms of scattering coefficients and scattering phase functions (SPFs) of the contributing components as follows [32]:

$$b\bar{\beta}(\psi) = b_w\bar{\beta}_w(\psi) + b_{\text{NAP}}\bar{\beta}_{\text{NAP}}(\psi) + b_{\text{Chl}}\bar{\beta}_{\text{Chl}}(\psi), \quad (17)$$

where $\bar{\beta}(\psi)$ is the SPF of sea water. The SPF of pure sea water, $\bar{\beta}_w$, has been well studied and, for our simulations, is taken from [31]. In contrast to the SPF of pure sea water, SPFs of nonalgal and chlorophyllic particles are not well established and show high variability with the water types because of the diversity of size distributions, refractive indices, and shape anisotropies of particles [6]. The most commonly used SPF is Petzold's average-particle phase function, derived from eight VSF measurements carried out by Petzold in San Diego Harbor [33,34]. However, Petzold's phase function results in a constant backscattering ratio of 0.0183, thereby prohibiting application of variable $\bar{b}_{b\text{Chl}}$ values [which decrease with increasing [Chl]; see Eq. (15)].

To meet this requirement for the backscattering ratio, we employed the phase functions given by the Fournier and Forand (FF) analytic expression [35], which is physically based on Mie theory and

has reasonable assumptions about the index of refraction and particle size distribution of oceanic particles [34]. With the use of the FF analytical expression, phase functions with the desired backscattering ratios can be generated by setting the real index of refraction of the particles, n_p , and the Junge slope parameter of their assumed distribution, μ_p . Thus, $\bar{\beta}_{\text{Chl}}$ used in our simulations are generated as FF phase functions by setting $n_{p\text{Chl}}$ to a fix value of 1.06 while varying the $\mu_{p\text{Chl}}$ values to achieve the desired $\bar{b}_{b\text{Chl}}$ values, as described in [29,34]. It should be noted here that the shape of the $\bar{\beta}_{\text{Chl}}$ obtained with the FF phase functions is very similar to that of Morel *et al.* [5] obtained through the T -matrix method (assuming randomly oriented spheroidal particles for all [Chl] levels used in our simulations). $\bar{\beta}_{\text{NAP}}$ is also computed through the FF expression by setting $n_{p\text{NAP}}$ and $\mu_{p\text{NAP}}$ to 1.1 and 3.58, respectively, to give a backscattering ratio of 0.0183 as in [34]. Figure 1 shows FF scattering phase functions with a backscattering ratio of 0.0045 (red) used for algal particles with [Chl] = 10 mg/m³, with a backscattering ratio of 0.007 (green) used for algal particles with [Chl] = 1 mg/m³, and with a backscattering ratio of 0.0183 (blue) used for NAP, together with the well-known Petzold's average-particle phase function for comparison.

3.2. Input Parameters for Simulation

IOP input parameters for the simulation are generated as independent random variables with a uniform distribution in the prescribed ranges. These selected ranges of the input parameters comprehensively cover the realistic synoptic scale water conditions for typical coastal waters [36]. In addition, as input parameters are each generated independently from one another, the resulting input dataset truly represents the conditions of the coastal waters, in which constituents of the water body vary independently. Table 1 describes the ranges of the input

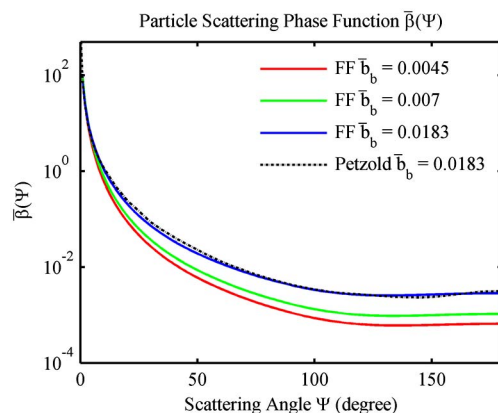


Fig. 1. (Color online) SPFs of particles used in simulations: FF $\bar{b}_b = 0.0045$ (red) is the SPF with a backscattering ratio of 0.0045, used for algal particles with [Chl] = 10 mg/m³, FF $\bar{b}_b = 0.007$ (green) is used for algal particles with [Chl] = 1 mg/m³, FF $\bar{b}_b = 0.0183$ (blue) is used for NAP, and Petzold's $\bar{b}_b = 0.0183$ (black dotted line) is Petzold's average-particle phase function.

parameters used in the simulation. With these assumed parameters, total absorption of the water at 412 nm, $a(412)$, is in the range 0.1–2.3 m^{-1} , the total particulate backscattering coefficient varies from 0.001 to 0.104 m^{-1} , and $\omega(\lambda)$ values are in the range of 0.005 to 0.3.

Remote sensing reflectance, R_{rs} , water-leaving radiance, L_w , and sea surface reflectance, ρ , were computed with Hydrolight with the following criteria using the IOP parameters specified above:

6 wavelengths: 412, 443, 491, 551, 668, and 753 nm
 9 solar zenith angles, θ_s : 0 to 80° at 10° intervals
 9 sensor zenith angles, θ_v : 0 to 80° at 10° intervals
 13 relative azimuth angles, ϕ : 0 to 180° at 15° intervals
 Wind speed, W : 5 m/s with cloud free skies for the dataset of remote sensing reflectance and radiance.

The three angles used as simulation inputs are defined as follows: solar zenith angle, θ_s , and sensor zenith angle, θ_v , are the angles between the zenith line pointing upward and the directions of the Sun and the sensor, respectively; the relative azimuth angle, ϕ , is defined as the angular difference between the sensor azimuth angle and the solar azimuth angle (i.e., the relative azimuth is $\phi = 0^\circ$ when the sensor is in opposition to the Sun and $\phi = 180^\circ$ when the Sun is exactly behind the sensor).

In our simulations we modeled the water as a homogeneous and infinitely deep medium for the sake of simplicity; therefore, this modeling is applicable only to the optically deep waters where bottom reflectance is negligible. Only elastic scattering was considered, and Raman inelastic scattering and fluorescence emission were not included. However, exclusion of Raman inelastic scattering has only a negligible impact on the accuracy of the modeling because of the relatively high particulate concentrations considered [5]. Chlorophyll fluorescence should not have an impact on the output of water-leaving radiance, because the selected wavelengths are far from the fluorescence emission peak (located around 685 nm) [37]. The Hydrolight standard quad layout, which essentially provides 10° resolution in the ze-

nith (θ) and 15° in the azimuth (ϕ) direction, was used. Hydrolight's built-in clear sky radiance model of Harrison and Coombes [38] and irradiance model of Gregg and Carder [39] were employed. Other atmospheric conditions such as sea-level pressure, relative humidity, horizontal visibility, and ozone concentration are set at default values, which are described in the Hydrolight 5 technical documentation [22,24].

3.3. Simulation Results and Analysis

In general, $R_{rs}(\lambda)$ is strongly correlated with $\omega(\lambda)$, as is known from the previous studies [6,10,17]. However, the value of $R_{rs}(\lambda)$ for a given value of $\omega(\lambda)$ does vary with the illumination and viewing geometries (i.e., solar and sensor angles) as discussed in Section 2. Figure 2 shows the simulated $R_{rs}(\lambda)$ data as a function of $\omega(\lambda)$ for the three conditions of solar and viewing angles at 412 and 551 nm. It is observed that the relationships between $R_{rs}(\lambda)$ and $\omega(\lambda)$ have a strong dependency on solar angles at low relative azimuth (ϕ) angles and that the dependency becomes gradually weaker with increasing ϕ values.

Using the simulated $R_{rs}(\lambda)$ and $\omega(\lambda)$ data, we computed the sets of tabulated coefficients α_i for the gridded values of θ_v , θ_s , ϕ , and λ according to Eq. (4). For each grid, we used 500 data points of R_{rs} and ω in a third order polynomial least-mean-square fitting procedure to produce the coefficients corresponding to the respective geometries and wavelengths. Table 2 shows the coefficients α_i for the nadir viewing and solar angles that are routinely employed in the estimation of $R_{rs}(\lambda)$ from $\omega(\lambda)$.

Figure 3 and Fig. 4 illustrate the variability of the coefficients α_i for the whole range of viewing and illumination geometries. Figure 3 highlights the dependency of the coefficients α_i on the solar and the sensor's zenith angles while the relative azimuth angle (ϕ) is kept constant at 90°, at which *in-situ* above-water measurements are usually performed in order to minimize sky and Sun glint. In the figure, variations in both contour structure and color intensity are observed for the coefficient α_i images of the different wavelengths, thereby confirming the wavelength dependency of the R_{rs} – ω relationship. Figure 4 also shows the variability of the coefficients α_i with respect to ϕ (x axis) and θ_s (y axis), where θ_v is kept constant at 40° for the same wavelengths as in Fig. 3.

4. Assessment of the Bidirectional Correction Algorithm

4.1. Theoretical Analysis

Based on the simulated dataset, we carried out the assessment of the bidirectional correction performed with the proposed model (hereafter referred to as the CCNY algorithm) as well as with the current operational algorithm [5] (referred to as the MG algorithm). It should be noted that although the MG algorithm is used operationally by current

Table 1. Ranges of the IOP Model Input Parameters Used in the Simulations

Parameters	Range
[Chl]	1 ~ 10 mg/m ³
$a_y(400)$	0 ~ 2 m ⁻¹
C_{NAP}	0.01 ~ 2.5 mg/m ³
S_y	0.01 ~ 0.02 nm ⁻¹
S_{NAP}	0.007 ~ 0.015 nm ⁻¹
$a_{NAP}^*(400)$	0.02 ~ 0.1 m ² /g
$b_{NAP}^*(550)$	0.5 ~ 1 m ² /g
γ_{chl}	0.1 ~ 1.6
γ_{NAP}	0.5 ~ 2
p	0.1 ~ 0.5

All parameters are randomly generated in the prescribed ranges with a uniform distribution.

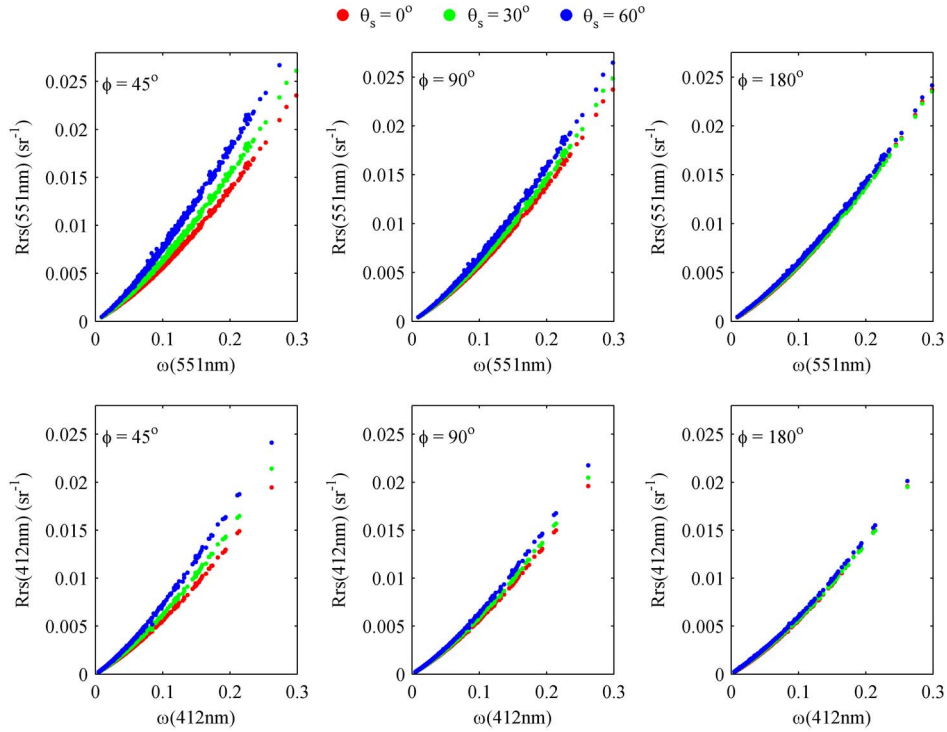


Fig. 2. (Color online) $Rrs(\lambda)$ with respect to $\omega(\lambda)$ at viewing angle $\theta_v = 40^\circ$ for $\lambda = 551$ nm (top row) and $\lambda = 412$ nm (bottom row) and for the relative azimuth angles $\phi = 45^\circ, 90^\circ$, and 180° (from left to right). Simulations are shown for the three λ solar zenith angles $\theta_s = 0^\circ$ (red), 30° (green), and 60° (blue).

above-water and satellite data processing [40] for bi-directional effect correction regardless of the water type, it was initially developed for case 1 water conditions. Thus, this theoretical analysis mainly intends to identify the amount of deviation induced by the case 1 optimized bidirectional algorithm in typical coastal water conditions. In the following analysis we focus on $Rrs(\lambda)$ for a fixed viewing angle ($\theta_v = 40^\circ$) at which the sea-based above-water radiance measurements are usually performed [41,42]. The solar zenith angle ranges from 20° to 70° , and the relative azimuth angle, ϕ , from 60° to 180° . These solar zenith and relative azimuth angle ranges cover the realistic conditions in which above-water measurements can be performed with the relatively low contamination from environmental effects [15].

In our assessments, simulated remote sensing reflectance at various viewing and illumination geometries, $Rrs(\theta_v, \theta_s, \phi, \lambda)$, is initially translated into nadir remote sensing reflectance, $Rrs(\theta_v = 0, \theta_s = 0, \phi = 0, \lambda)$, using both CCNY and MG algorithms. Then those nadir remote sensing reflectance values,

$Rrs(\theta_v = 0, \theta_s = 0, \phi = 0, \lambda)$, obtained with the CCNY algorithm (from here on denoted as $Rrs_{\text{retrieved(CCNY)}}^0$) and the MG algorithm (denoted as $Rrs_{\text{retrieved(MG)}}^0$) are compared to the exactly corresponding simulated nadir remote sensing reflectance value, denoted as Rrs_{actual}^0 . $Rrs_{\text{retrieved(CCNY)}}^0$ is calculated as follows:

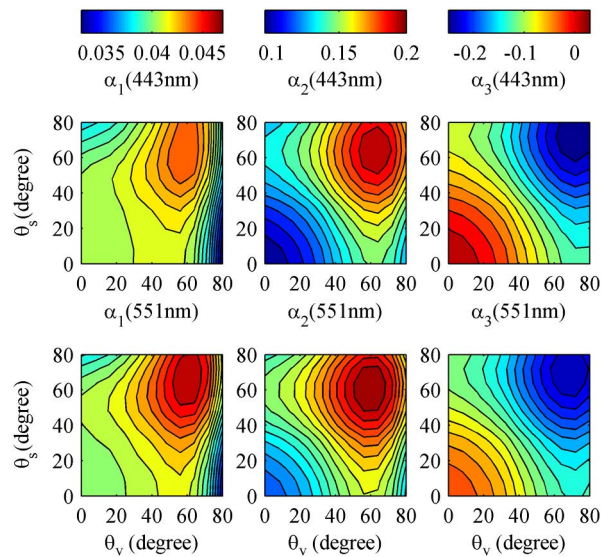


Fig. 3. (Color online) Color plots of the coefficients $\alpha_i(\theta_s, \theta_v, \phi, \lambda)$, sr^{-1} : α_1 (first column), α_2 (second column), and α_3 (third column) are shown as a function of the sensor's zenith angle θ_v (x axis) and the solar zenith angle θ_s (y axis) while the relative azimuth angle ϕ is kept constant at 90° . The coefficients are shown for two wavelengths: $\lambda = 443$ nm (top row) and 551 nm (bottom row).

Table 2. Coefficients α_i , sr^{-1} , for the Nadir Viewing and Solar Angles

	λ (nm)				
	412	443	491	551	668
α_1	0.04115	0.04073	0.04030	0.04023	0.03879
α_2	0.10186	0.09755	0.11102	0.1171	0.09425
α_3	0.01986	0.002898	0.00524	-0.01355	0.09660

$\theta_v = 0^\circ$ and $\theta_s = 0^\circ$.

(i) $\omega(\lambda)$ is derived by fitting $\text{Rrs}(\theta_v, \theta_s, \phi, \lambda)$ to the respective $\alpha_i(\theta_s, \theta_v, \phi, \lambda)$ of Eq. (4); (ii) $\text{Rrs}_{\text{retrieved(CCNY)}}^0$ is then calculated by plugging $\omega(\lambda)$ obtained in the first step into Eq. (4) again, together with $\alpha_i(\theta_s = 0, \theta_v = 0, \phi = 0, \lambda)$.

However, in the case of the MG algorithm, prior estimation of [Chl] is required. This estimation of [Chl] is carried out by using an empirical formula that relates the ratio of the water-leaving radiances of the blue and green bands to [Chl] [5,41]. In the MG algorithm considered in this study, we used the empirical formula (OC2) developed as a product of the SeaWiFS Bio-optical Algorithm Mini Workshop (SeaBAM) [43]. This empirical formula is also adopted in the operational AERONET Ocean Color (OC) data processing for ocean color satellite data validation activities. The formula is defined as

$$\text{Chl} = -0.0929 + 10^{0.2974 - 2.2429X + 0.8358X^2 - 0.0077X^3}, \quad (18)$$

where

$$X = \log_{10} \left(\frac{\text{Rrs}(490)}{\text{Rrs}(555)} \right). \quad (19)$$

The use of this blue–green ratio [Chl] estimation algorithm [Eq. (18)] remains highly questionable for the optical properties typically retrieved in coastal waters [44,45]. Nevertheless, the focus of our analysis is to identify the deviation induced by the whole operational bidirectional correction process. Thus, this algorithm has been used here without modifications or adjustments. On the other hand, even if [Chl] values are retrieved with reasonable accuracy, the current operational MG algorithm will still suffer from its single particle type assumption, in which the contributions of scattering from the mineral rich NAP (which are typical for coastal water

conditions) are not considered. In our simulations we assumed for Eq. (19) $\text{Rrs}(490) \approx \text{Rrs}(491)$ and $\text{Rrs}(555) \approx \text{Rrs}(551)$, which almost did not affect [Chl] values.

Based on the estimated [Chl] [Eq. (18)], f/Q factors are acquired from the lookup tables [5]. After that, $\text{Rrs}_{\text{retrieved(MG)}}^0$ is calculated as

$$\begin{aligned} \text{Rrs}_{\text{retrieved(MG)}}^0 &= \frac{\mathfrak{R}_0}{\mathfrak{R}(\theta_v, W)} \times \frac{f_0(\lambda, \text{Chl})}{Q_0(\lambda, \text{Chl})} \\ &\times \frac{Q(\theta_s, \theta_v, \phi, \lambda, \text{Chl})}{f(\theta_s, \lambda, \text{Chl})} \\ &\times \text{Rrs}(\theta_s, \theta_v, \phi, \lambda), \end{aligned} \quad (20)$$

where \mathfrak{R}_0 denotes the particular value of \mathfrak{R} when $\theta_v = 0$. In the same way, f_0 denotes the particular value of f when $\theta_s = 0$, and Q_0 denotes the Q value when $\theta_v = 0$ and $\theta_s = 0$. It is worth noting that the parameters f and Q of Eq. (20) are computed based on typical oceanic case 1 water optical properties.

Then, both $\text{Rrs}_{\text{retrieved(CCNY)}}^0$ and $\text{Rrs}_{\text{retrieved(MG)}}^0$ are compared to $\text{Rrs}_{\text{actual}}^0$, and the following statistical indicators are calculated. The absolute percent difference for each matchup, denoted as δ_i , is

$$\delta_i = 100 \times \frac{|x_i - y_i|}{x_i}. \quad (21)$$

The absolute average percent difference (AAPD) is defined as

$$\text{AAPD} = \frac{1}{N} \sum_{i=1}^N \delta_i, \quad (22)$$

and the average percent difference (APD) is

$$\text{APD} = \frac{100}{N} \sum_{i=1}^N \frac{x_i - y_i}{x_i}, \quad (23)$$

where x stands for $\text{Rrs}_{\text{actual}}^0$ and y for either $\text{Rrs}_{\text{retrieved(CCNY)}}^0$ or $\text{Rrs}_{\text{retrieved(MG)}}^0$. In the comparisons, the statistical indicator AAPD provides the information regarding the dispersion, while APD can be used to assess the expected bias between the compared datasets.

Those comparisons have been carried out for (i) $\text{Rrs}_{\text{actual}}^0$ and corresponding Rrs (before the bidirectional effect is removed) in order to make the assessment of the bidirectional variations of the assumed water types for the viewing and illumination configurations mentioned above (i.e., $\theta_v = 40^\circ$, $20^\circ \leq \theta_s \leq 70^\circ$, and $60^\circ \leq \phi \leq 180^\circ$), (ii) $\text{Rrs}_{\text{actual}}^0$ and $\text{Rrs}_{\text{retrieved(MG)}}^0$ to identify the relative error resulting from the use of the case 1 water optimized correction algorithm for case 2 water conditions, and (iii) $\text{Rrs}_{\text{actual}}^0$ and $\text{Rrs}_{\text{retrieved(CCNY)}}^0$ to obtain the statistics for the error induced in the correction processes.

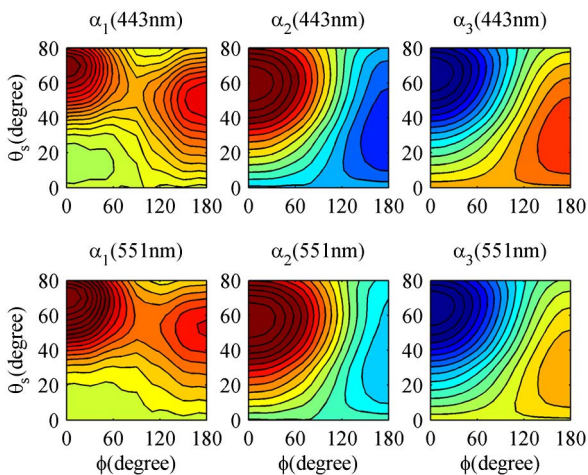


Fig. 4. (Color online) α_1 (first column), α_2 (second column), and α_3 (third column), sr^{-1} , are shown as a function of ϕ (x axis) and the solar zenith angle θ_s (y axis) while the sensor's viewing angle θ_v is kept constant at 40° . Color intensity values are the same as in Fig. 3.

Figures 5(a)–(e) show the comparisons between $Rrs_{\text{retrieved}}^0$ and Rrs_{actual}^0 at 412, 443, 491, 551, and 668 nm, respectively, for the viewing and illumination configurations mentioned above. It is observed that the comparisons show high AAPD values (6.26% to 9.5%) and APD values (2.8% to 9.4%) at all the wavelengths with the MG algorithm, and regression line slopes between $Rrs_{\text{retrieved(MG)}}^0$ and Rrs_{actual}^0 are 1.05, 1.03, 0.98, 0.93, and 0.97, respectively, for 412, 443, 491, 551, and 668 nm wave-

lengths. The dispersion between the two datasets is observed to be relatively smaller for the shorter wavelengths (412 and 443 nm) and is largest at 551 nm.

By contrast, the comparisons between $Rrs_{\text{retrieved(CCNY)}}^0$ and Rrs_{actual}^0 exhibit much smaller AAPD (0.42%–0.8%) and APD (0.054%–0.55%) at all wavelengths. The regression lines between $Rrs_{\text{retrieved(CCNY)}}^0$ and Rrs_{actual}^0 are very close to the 1:1 line for all wavelengths. Moreover, the retrieved

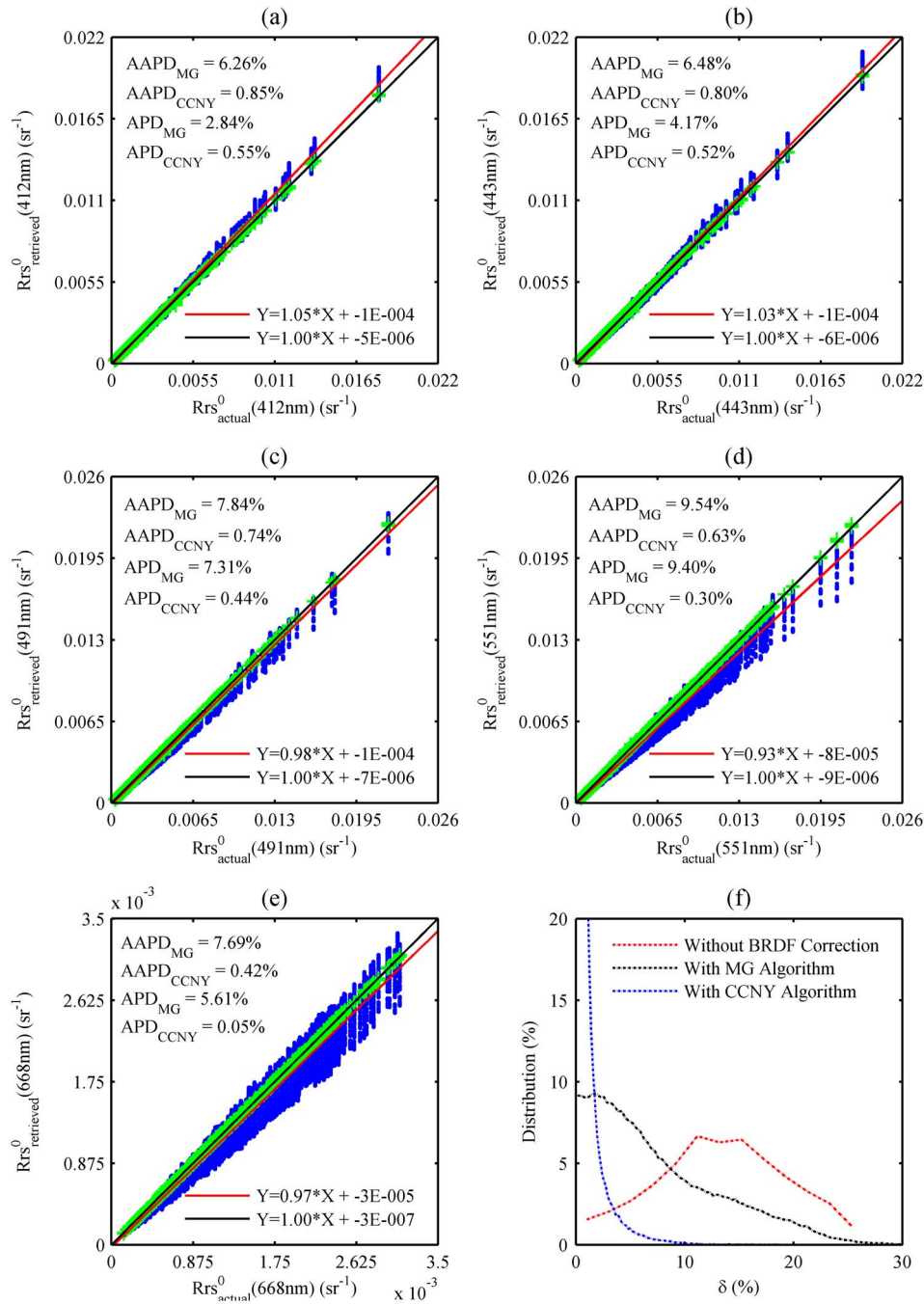


Fig. 5. (Color online) Comparisons between Rrs_{actual}^0 and $Rrs_{\text{retrieved}}^0$ derived with MG (blue dots) and CCNY (green dots) algorithms for $\theta_i = 40^\circ$, $20^\circ \leq \theta_s \leq 70^\circ$, and $60^\circ \leq \phi \leq 180^\circ$ at (a) 412, (b) 443, (c) 491, (d) 551, and (e) 668 nm. Regression lines between $Rrs_{\text{retrieved(MG)}}^0$ and Rrs_{actual}^0 are shown in red, and those of $Rrs_{\text{retrieved(CCNY)}}^0$ are shown in black. (f) Distribution of the absolute percent difference, δ , values between Rrs_{actual}^0 and $Rrs_{\text{retrieved(MG)}}^0$ (black), and $Rrs_{\text{retrieved(CCNY)}}^0$ (blue) for each matchup.

differences between $Rrs_{\text{retrieved(CCNY)}}^0$ and Rrs_{actual}^0 , which mostly originate from the least-mean-square fitting procedure, are found to be negligible in comparison with the actual bidirectional variation, which is generally in the range of 10%–20%, as can be readily seen in Fig. 5(f). In this figure, the histogram of the absolute percent difference values combined for all wavelengths shows that δ values between Rrs_{actual}^0 and Rrs without BRDF correction are in the range of 2.3%–25% and AAPD is around 13.5%, which is consistent with previous studies [6,7]. In addition, it can be seen that without the BRDF correction, only 9.5% of the data have absolute percent difference (δ) values within 5%, and more than two-thirds of the data have δ values greater than 10%. These results demonstrate the importance of the bidirectional effect correction in the retrieval process if the water-leaving radiances (and remote sensing reflectances) are to be retrieved within the ocean color sensor community's targeted accuracy level (i.e., less than 5% uncertainty) for above-water measurements.

Similarly, δ values between Rrs_{actual}^0 and $Rrs_{\text{retrieved(MG)}}^0$ range from 0% to 27%. Nevertheless, AAPD is reduced to 7.56%. Moreover, it was observed that 43% and 70.6% of the data set have δ values less than 5% and 10%, respectively. These results show that the bidirectional effect is reduced with the use of the MG correction algorithm and that using the MG algorithm in coastal water conditions can still offer better retrievals than not correcting at all. However, 57% of the data have δ values greater than 5%, and thus these results also outline the need for the bidirectional correction algorithm optimized for case 2 water conditions. On the other hand, the distribution curve of δ values between Rrs_{actual}^0 and $Rrs_{\text{retrieved(CCNY)}}^0$ shows a much narrower range, and 98.4% of the data have δ values less than 5%. The mean of the δ value is also drastically reduced to 0.69%, demonstrating that the CCNY BRDF correction algorithm works very well with the simulated dataset.

4.2. Noise Sensitivity Analysis

Water-leaving radiances retrieved from above-water radiometric measurements are subject to uncertainty that arises from geophysical noise, such as rapid changes in environmental conditions, and Sun and sky glints, which are randomly fluctuating from the effects of surface waves. The current above-water radiometry processing algorithm employs the glint filtering method, in which only the lowest of multiple successive total sea radiance measurements taken within a short period are utilized in the processing of Rrs in order to minimize the effect of the glint [15,41]. Such practices may result in the residual random component affecting the retrieved Rrs . Removal of the reflected sky radiance can also lead to residual errors, which are not taken into account by the removal model [15]. For the satellite data, errors can arise from inaccuracies in atmospheric cor-

rection or from other sources. The analysis of such residual errors resulting from each step of the data processing procedures is beyond the scope of this paper and deserves a dedicated study because of the importance of the topic. Here, our analysis simply intends to identify the proposed model's sensitivity to the noise, in other words, to verify whether the proposed model can still offer meaningful corrections (i.e., whether output $Rrs_{\text{retrieved}}^0$ are closer to corresponding Rrs_{actual}^0 than $Rrs(\theta_v, \theta_s, \phi, \lambda)$ are) when Rrs measurements are contaminated by geophysical noise, and to determine the threshold of noise level with respect to the Rrs signal. Since the proposed model performs the correction at each wavelength independently and modeling errors at each wavelength are much lower than assumed noise levels, the model's sensitivity to the noise at each wavelength can be evaluated from this analysis.

In order to test the applicability of the CCNY algorithm in the above-water correction procedures, we first added synthetic noise signals to the $Rrs(\theta_v, \theta_s, \phi, \lambda)$ values before the BRDF correction was applied. Then, these noise-contaminated $Rrs(\theta_v, \theta_s, \phi, \lambda)$ values are converted to nadir remote sensing reflectances, using the CCNY algorithm. After that, noise-contaminated $Rrs_{\text{retrieved(CCNY)}}^0$ values are compared to the respective Rrs_{actual}^0 values as in the previous section. For this analysis, synthetic noise signals are independently generated for each $Rrs(\theta_v, \theta_s, \phi, \lambda)$ value as random numbers with a Gaussian distribution with zero mean and standard deviation proportional to the corresponding Rrs values.

Figure 6 shows the distributions of δ values (combined for all wavelengths) between Rrs_{actual}^0 and noise-contaminated $Rrs_{\text{retrieved(CCNY)}}^0$ values for three levels of noise (5%, 10%, and 15%) together with the distribution of δ values for Rrs without a BRDF correction. It was found that AAPD values of the retrievals are increased to 4.0%, 7.9%, and 12.9%, respectively, for the dataset with 5%, 10%, and

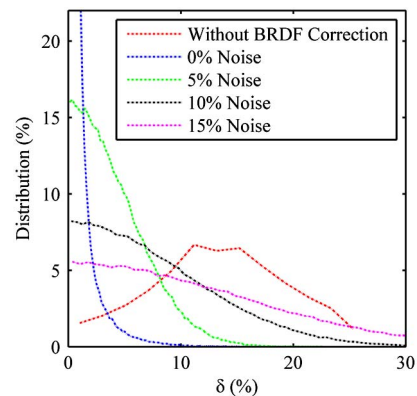


Fig. 6. (Color online) Distribution of the absolute percent difference (δ) values for $Rrs_{\text{retrieved(CCNY)}}^0$ infected with four different noise levels: 0% (blue), 5% (green), 10% (black), and 15% (magenta). The red curve corresponds to the case where Rrs is not corrected for BRDF. Illumination and viewing configurations are the same as in Fig. 5.

15% noise levels. Although retrieval performances are lower with the introduction of noise to the signal, δ values for all noise levels are shifted toward smaller values compared to the δ values for Rrs without BRDF correction. Thus, it shows that even noise-contaminated Rrs measurements can still considerably benefit from bidirectional correction.

5. Bidirectional Reflectance Distribution Correction of Above-Water Measurements

5.1. LISCO Instrumentation

As was mentioned above in the introduction, performance of the proposed BRDF correction approach was also evaluated by measurements obtained at LISCO. LISCO combines a multispectral SeaPRISM (Cimel, France) instrument as a part of AERONET-OC Network [46] with a colocated hyperspectral HyperSAS (Satlantic, Canada) radiometric system. Both instruments are positioned on a retractable tower with an elevation of 12 m. They were installed

are achieved for 180 channels regularly spaced between 305 and 905 nm. Two radiance sensors are mounted on the same instrument plate as the SeaPRISM system and have a full angle field of view of 3° . But, unlike SeaPRISM, the sensors point exactly westward all the time. As a result, the relative azimuth angle ϕ changes throughout the day, encompassing the whole range from 0° to 180° . HyperSAS measurement sequences are also executed every 30 min, as in the case of SeaPRISM, and each sequence takes 2 min. Within 2 min, the number of measurements acquired by HyperSAS system varies from 45 to 80 for L_t and from 50 to 220 for L_{sky} and E_d measurements depending on ambient light conditions.

5.2. Method and Data Processing

Remote sensing reflectance spectra, $Rrs(\lambda)$, for a specific viewing and illumination condition are calculated as described in [16] as follows:

$$Rrs(\theta_s, \theta_v, \phi, \lambda) = \frac{L_t(\theta_s, \theta_v, \phi, \lambda, W) - \rho(\theta_s, \theta_v, \phi, W)L_{\text{sky}}(\theta_s, \theta_v'', \phi, \lambda)}{E_d(\theta_s, \lambda)} \quad (24)$$

on the LISCO platform in October 2009 and have been continuously providing data since then.

The SeaPRISM system consists of CE-318 Sun photometers modified to meet requirements for above-water radiometry. The photometers perform radiance measurements with a full-angle field of view of 1.2° to determine the total radiance from the sea, $L_t(\theta_s, \theta_v, \phi, \lambda)$, and the sky, $L_{\text{sky}}(\theta_s, \theta_v'', \phi, \lambda)$, where $\theta_v'' = 180 - \theta_v$. Thanks to the rotating feature of SeaPRISM, ϕ is always set to 90° regardless of the Sun position, and θ_v is set at 40° . These values were determined in order to minimize the perturbations resulting from the Sun glint off the sea surface [16] and the deployment superstructure itself or its shadow [41]. The SeaPRISM system configuration of LISCO performs ocean color measurements at the 412, 443, 491, 551, 668, 870, and 1018 nm center wavelengths. These center wavelengths were selected to be as close as possible to the bands of current ocean color earth observation systems in order to support essential validation activities. Measurement sequences are executed every 30 min within ± 4 h of 12:00 PM local time. Each measurement sequence, which consists of three sky (L_{sky}) and eleven sea (L_t) radiance data acquisitions, takes approximately 6 min.

The hyperspectral measurements are achieved by a HyperSAS system providing high precision measurements of $L_t(\theta_s, \theta_v, \phi, \lambda)$, $L_{\text{sky}}(\theta_s, \theta_v'', \phi, \lambda)$, and downwelling spectral irradiance $E_d(\theta_s, \lambda)$. The radiance and irradiance measurements of HyperSAS

Following our previous study [15], the total radiance (L_t) utilized in Eq. (24) for the SeaPRISM instrument is obtained from Level 1.5 cloud screened data of AERONET-OC data distribution [47]. In the case of HyperSAS, L_t is calculated by averaging the lowest 5% of the sea radiance measurements taken during the 2 min data acquisition time. HyperSAS performs 45 to 80 total sea radiance measurements during its 2 min data acquisition window, depending on the brightness of the total radiances being obtained. Taking the lowest 5% allows the averaging of at least two measurements during every cycle of 2 min data acquisition for further processing. On the other hand, the sky radiance, L_s , is determined by simply averaging all sky radiance measurements. The sea surface reflection coefficient, $\rho(\theta_s, \theta_v, \phi, W)$, for the desired exact viewing and illumination geometries and the wind speed are obtained by performing a linear interpolation on the reflection coefficient dataset acquired through Hydrolight's simulations described in Section 3. Input surface wind speed data for each data acquisition cycle are acquired from the National Weather Service. Downwelling irradiance, $E_d(\lambda)$, measurements are acquired by the vertically installed irradiance sensor, part of the HyperSAS system and used in the calculation of $Rrs(\lambda)$ for both HyperSAS and SeaPRISM systems.

5.3. Assessment of the Bidirectional Reflectance Distribution Function via LISCO Data

One of the major advantages of the LISCO instrumentation set is that HyperSAS and SeaPRISM

instruments acquire data almost concurrently but with different viewing geometries as the day progresses, except for the time when the Sun is exactly south when both instruments point west. As both instruments make measurements within a 10 min window, it is reasonable to consider that the composition of the water constituents within that time window remains the same. Ideally, observed variations in the water-leaving radiances acquired by the two instruments can be attributed to the variations due to the BRDF only. Hence, the assessments of the performance of the BRDF corrections can be made by comparing the nadir remote sensing reflectance obtained from SeaPRISM [denoted as $Rrs_{Spr}^0(\lambda)$] and from HyperSAS [denoted as $Rrs_{HS}^0(\lambda)$]. However, it should be pointed out that directional fluctuations in the measured sea radiance are also induced by the Sun and sky light reflections on the ruffled surface, which in the end may create significant uncertainties in the retrieved water-leaving radiance [15,48]. Therefore, it is of paramount importance to filter out the data corrupted by unexpected environmental effects or any stochastic artifacts beforehand. The filtering procedure for quality assurance has already been developed for the SeaPRISM system in the framework of AERONET-OC distribution [46], and all the data we used in this study are quality-checked level 1.5 cloud-screened data [47]. Similarly, a specific HyperSAS data filtering procedure has been developed by us independent of SeaPRISM [15], and those procedures were closely followed in this study for the data processing. Then, hyperspectral HyperSAS data were integrated with the sensor relative spectral response function of each SeaPRISM band in order to produce equivalent data for both systems. The data involved were restricted to SeaPRISM measurement sequences taken within ± 10 min of HyperSAS sequence intervals. In addition, findings from our previous study suggest that the contamination by en-

vironmental effects of the retrieved water-leaving radiance becomes sensitive for $\phi < 60^\circ$ regardless of the Sun's elevation, with uncertainties higher than 5% [15]. As a consequence, it has been decided to eliminate HyperSAS measurements taken with $\phi < 60^\circ$ from the analysis.

In the following, we first show the intercomparisons between the remote sensing reflectance of HyperSAS and SeaPRISM before the bidirectional effect are corrected [denoted as $Rrs_{HS}(\lambda)$ and $Rrs_{Spr}(\lambda)$, respectively]. This comparison (see Fig. 7) allows us to make the assessment of the variation in two measurements before the bidirectional effects are removed. Second, we perform the comparisons between the final nadir remote sensing reflectance of both instruments [denoted as $Rrs_{HS}^0(\lambda)$ and $Rrs_{Spr}^0(\lambda)$] processed with both the CCNY and MG algorithms (see Fig. 8). Finally, we compare the final nadir remote sensing reflectance of both instruments processed with the CCNY algorithm (denoted as $Rrs_{retrieved(CCNY)}^0$) to those processed with the MG algorithm (denoted as $Rrs_{retrieved(MG)}^0$) (see Fig. 9). In the comparisons, because neither SeaPRISM nor HyperSAS data can be assigned as the reference, the following statistical indicators given in percentage points are used.

The absolute relative percent difference (ARPD) is defined as follows:

$$ARPD = \frac{200}{N} \sum_{i=1}^N \frac{|y_i - x_i|}{x_i + y_i}, \quad (25)$$

and the unbiased relative percent difference (URPD) is

$$URPD = \frac{200}{N} \sum_{i=1}^N \frac{y_i - x_i}{x_i + y_i}, \quad (26)$$

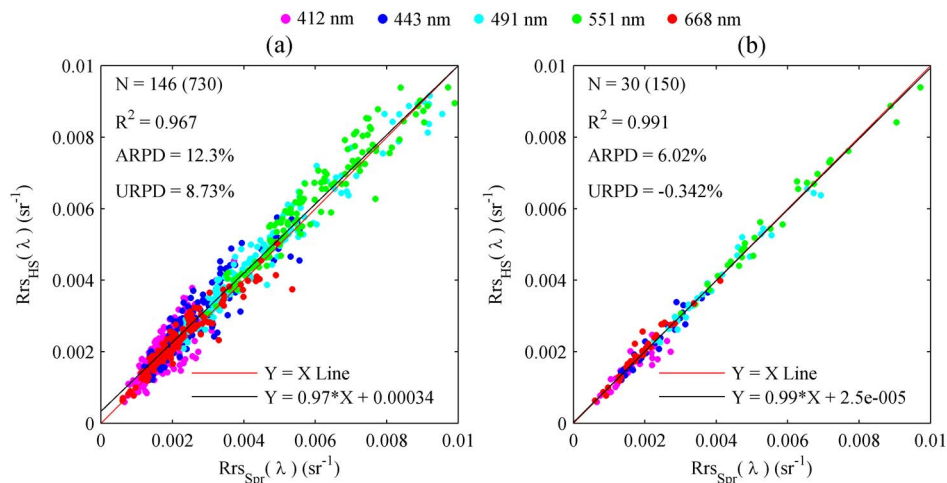


Fig. 7. (Color online) Intercomparisons of remote sensing reflectances (in sr^{-1}) derived from SeaPRISM and HyperSAS before correction for the bidirectional effect: (a) relative azimuth angles for HyperSAS observations are restricted in the $60^\circ \leq \phi \leq 180^\circ$ range; (b) relative azimuth angle range is restricted to $80^\circ \leq \phi \leq 100^\circ$. N is the total number of the comparisons, and the value in parentheses is the number of different measurement sequences used in the comparison.

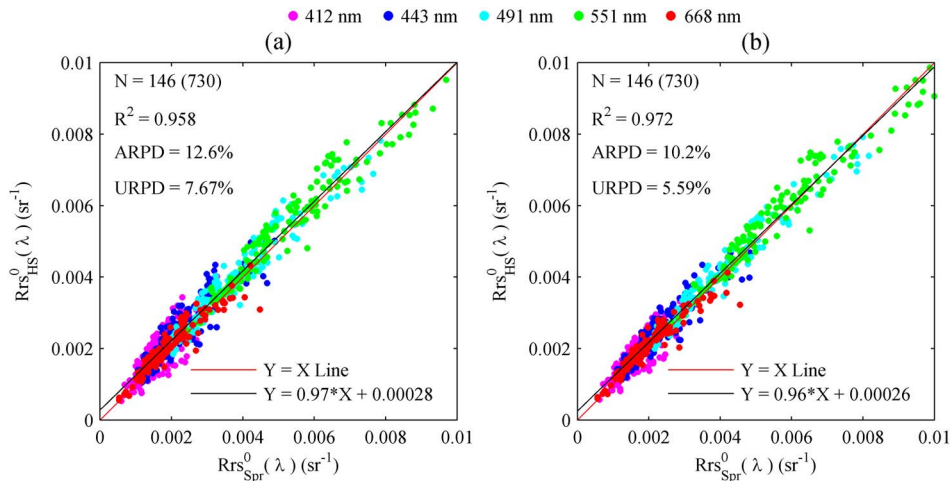


Fig. 8. (Color online) Intercomparisons of SeaPRISM and HyperSAS remote sensing reflectance measurements (in sr^{-1}) after the bidirectional effect is corrected: (a) processed with the MG algorithm, (b) processed with the CCNY algorithm. Relative azimuth angles, ϕ , for HyperSAS observations are the same as in Fig. 7(a).

where SeaPRISM data are taken as x and HyperSAS data are taken as y .

Figure 7(a) shows the comparison of remote sensing reflectance measurements of HyperSAS and SeaPRISM [$Rrs_{\text{HS}}(\lambda)$ and $Rrs_{\text{Spr}}(\lambda)$] before the bidirectional effect is removed for all the data used in this analysis. The comparison exhibits strong correlations between HyperSAS and SeaPRISM data, with the R^2 value around 0.967, and the regression line between two pieces of data is also very close to the 1:1 line. The URPD and ARPD values, which show the bias and dispersion between two pieces of data, are 8.73% and 12.3%, respectively. However, when the relative azimuth angle range for the HyperSAS instrument is restricted to the $80^\circ \leq \phi \leq 100^\circ$ range [see Fig. 7(b)], the URPD and ARPD values are reduced down to -0.342% and 6.02% , respectively. In addition, the R^2 value is increased to 0.991, and the regression line comes closer to the 1:1 line, showing a better consistency between the two measurements. In fact, with this restricted relative azimuth range, HyperSAS and SeaPRISM measurements are taken for an azimuth within $\pm 10^\circ$, and thus bidirectional effects for the measurements of both systems are about the same. Therefore, it can be considered that this statistical difference between the two comparisons arises from the bidirectional variation of the water-leaving radiance as well as from possible residual Sun and sky glint effects. In fact, these residual glints may be considered to have the same effect as the noise on the correction procedures, as shown in Section 4.2.

Comparisons of the $Rrs_{\text{HS}}^0(\lambda)$ and $Rrs_{\text{Spr}}^0(\lambda)$ processed with the MG and CCNY algorithms are shown in Figs. 8(a) and 8(b), respectively. In the comparison of the $Rrs_{\text{HS}}^0(\lambda)$ and $Rrs_{\text{Spr}}^0(\lambda)$ processed with the MG algorithm, the URPD value is reduced down to 7.67%, showing a 1.06% reduction in relative percent difference compared to the same data not corrected for the bidirectional effects. However, its ARPD value is increased by 0.3% compared to the value before the

correction. The R^2 value is also observed to be reduced down to 0.958. These results indicate that the dispersion between the two data is somewhat increased by the MG correction procedure. This shows the inadequacy of bidirectional correction based on the assumption of case 1 water for the typical LISCO waters. On the other hand, comparison with the same data processed with the CCNY algorithm shows a reduction in both ARPD and URPD values (2.1% and 3.14%, respectively) with respect to the data not corrected for bidirectional effects, while R^2 is increased to 0.972. Therefore, this indicates that with the use of the CCNY bidirectional correction algorithm, dispersion between the two measurements resulting from the different viewing configuration can be reduced, thereby demonstrating the relevance and appropriateness of the CCNY bidirectional correction for the water-leaving radiance measured by the HyperSAS and SeaPRISM instruments in the moderately turbid waters of the LISCO site. It can also be observed that both ARPD and URPD values of the data corrected with the CCNY algorithm are lower than those corrected with the MG algorithm at every wavelength, showing 1.95% to 3.0% improvement in terms of ARPD and 1.65% to 2.65% in terms of URPD (see Table 3 for details).

Figure 9 shows the intercomparisons between $Rrs_{\text{retrieved(CCNY)}}^0$ and $Rrs_{\text{retrieved(MG)}}^0$. It is observed that the relative absolute percent difference between the output nadir remote sensing reflectance of the two algorithms ranges from 0% to 14.5%, where the largest difference found at 551 nm with the AAPD between the outputs of the two algorithms is 6.14%. The slopes between the output final nadir remote sensing reflectances of the two algorithms are 1.05, 0.95, and 0.905 for 412, 491, and 551 nm wavelengths, respectively, suggesting that the MG algorithm is overestimating the nadir remote sensing reflectances at 412 nm and underestimating them at 491 and 551 nm. It should be noted that comparisons carried out with the field measurement data

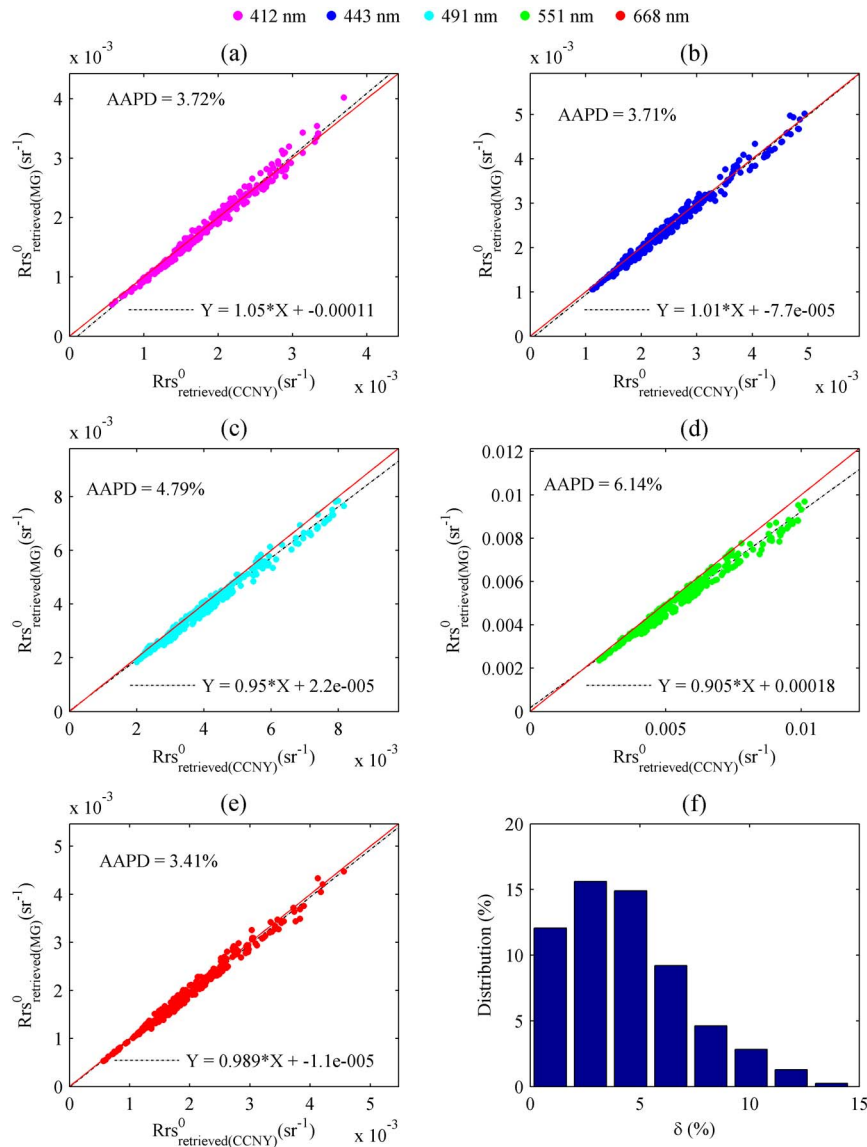


Fig. 9. (Color online) Intercomparisons between $Rrs^0_{\text{retrieved(CCNy)}}$ and $Rrs^0_{\text{retrieved(MG)}}$ at (a) 412 nm, (b) 443 nm, (c) 491 nm, (d) 551 nm, and (e) 668 nm. (f) Distribution of absolute percent difference (δ) between $Rrs^0_{\text{retrieved(CCNy)}}$ and $Rrs^0_{\text{retrieved(MG)}}$ for all wavelengths. Both HyperSAS and SeaPRISM data are plotted together.

illustrate similar slopes to those carried out with the simulated data set.

6. Application of the BRDF Correction Algorithm to MODIS Satellite Data

A previous study has confirmed that the LISCO site is appropriate for use in calibration/validation of the ocean color satellites in coastal waters [14]. In the study, we compared time series normalized water-leaving radiance (nLw) measurements obtained at LISCO with the ones derived from satellite data. That time series comparison performed with the use of a nine-month data period exhibited both qualitative and quantitative agreements between water-leaving radiances derived from LISCO measurements and satellite data, showing strong correlations and relatively low average percent differences between the datasets, especially at 443, 491, and

551 nm [14]. Similar to this previous study, matchup comparisons have been carried out between the *in situ* SeaPRISM and satellite $Rrs^0(\lambda)$ data for LISCO's location. $Rrs^0(\lambda)$ data of both *in situ* and satellite types are processed in the following two different ways: (i) with standard BRDF correction (the MG algorithm) and (ii) with the proposed CCNY algorithm. Then, *in situ* and satellite data matchup comparisons are carried out for both obtained datasets in order to assess merits and benefits of the proposed algorithm over the standard one.

We used the data from the MODIS onboard the *Aqua* satellite for the matchup and for the comparisons with the *in situ* data. MODIS (*Aqua*) Level 1 data for a 14-month period (October 2009 through December 2010) were acquired from the ocean color data distribution website [49]. These data were processed using the software package SeaDAS version

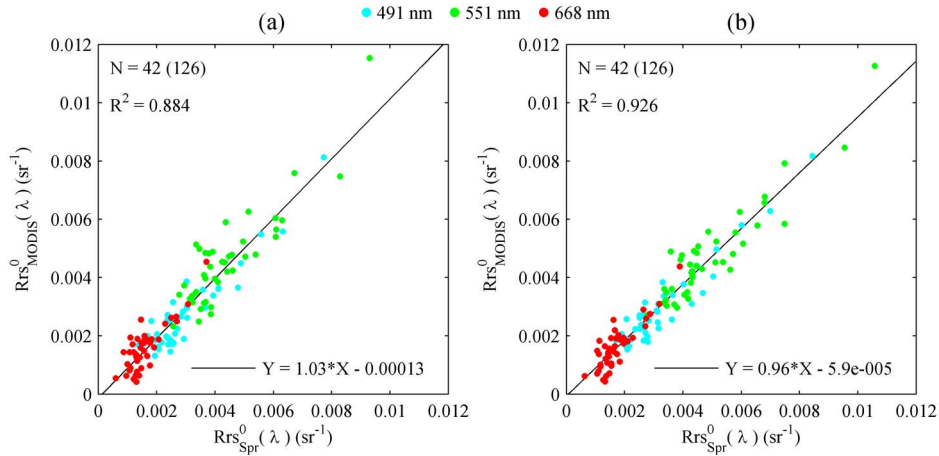


Fig. 10. (Color online) Scattering plots of the comparisons between MODIS and *in situ* data: (a) comparison between MODIS and SeaPRISM with MG BRDF processing, (b) comparison between MODIS and SeaPRISM with CCNY BRDF processing.

6.2 (which contains all of the final processing programs and the source code used for the OBPG's Ocean Color Reprocessing 2010) into two groups of Level 2 data files (one group is processed using the MG BRDF correction and another group with the CCNY BRDF correction) at the nominal 1 km resolution. Then we extracted the data of the 3 km × 3 km area centering the LISCO platform to create two time series of MODIS $Rrs^0(\lambda)$ data sets processed with the MG and CCNY BRDF correction algorithms. For data quality assurance purposes, Level 2 flags [i.e., land, cloud, high Sun glint, very low water-leaving radiance (cloud shadow), and atmospheric correction failure] were applied in the data extraction procedure. The average values of the 3 km × 3 km area are considered qualified for comparison with *in situ* data when at least 50% of the pixels are not affected by these standard flags. On the other hand, two sets of *in situ* SeaPRISM $Rrs^0(\lambda)$ data processed with the MG and CCNY BRDF corrections were selected from the measurements that passed the data filtering procedures [15] and taken within ±4 hours of the satellite overpass time for the LISCO location.

Subsequently, we compared the MODIS $Rrs^0(\lambda)$ datasets (processed using both the CCNY and MG algorithms for bidirectional correction), from here on

denoted as $Rrs^0_{MODIS}(\lambda)$, to the corresponding SeaPRISM ($Rrs^0_{Spr}(\lambda)$) datasets. Comparisons were carried out for both correction algorithms and statistics, such as AAPD, and coefficients of determination (R^2) have been obtained. A total of 42 MODIS and SeaPRISM matchups and comparisons were carried out. Sensor and solar zenith angles of MODIS data used in the comparisons are in the range of 5° to 56° and 20° to 60°, respectively, and therefore a wide range of illumination and viewing geometries are available to test the bidirectional corrections. Table 4 shows the resulting AAPD values from the comparison between $Rrs^0_{MODIS}(\lambda)$ and $Rrs^0_{Spr}(\lambda)$ data processed with the MG and CCNY algorithms.

In the comparisons of $Rrs^0_{MODIS}(\lambda)$ and $Rrs^0_{Spr}(\lambda)$ data, the CCNY algorithm exhibits noticeable improvements throughout the spectrum. The spectrally averaged AAPD between the two datasets is reduced about 3.15% with the use of the CCNY algorithm (see Table 4 for details). Figure 10 shows the scatterplots of the $Rrs^0_{MODIS}(\lambda)$ versus $Rrs^0_{Spr}(\lambda)$ data. Figure 10(a) shows the comparison of MODIS and SeaPRISM data, processed with the MG algorithm, while Fig. 10(b) shows the comparison of the same data processed with the CCNY algorithm. The three wavelengths 491, 551, and 668 nm are shown in the plots, and a stronger correlation (0.926) is observed

Table 3. Statistical Summary of the Intercomparisons of SeaPRISM and HyperSAS Remote Sensing Reflectance Measurements

		Wavelength (nm)					Spectral Average
		412	443	491	551	668	
Before BRDF correction	R^2	0.7(0.81)	0.85(0.94)	0.95(0.98)	0.96(0.98)	0.95(0.95)	0.967(0.991)
	ARPD	21(11.3)	16(5.81)	7.86(3.23)	5.9(3.12)	10.8(6.67)	12.3(6.02)
	URPD	12.1(-5.9)	11.6(-0.02)	5.18(0.66)	3.56(0.67)	7.48(4.21)	8.73(-0.34)
Corrected with MG algorithm	R^2	0.689	0.833	0.941	0.945	0.883	0.958
	ARPD	20.35	16.3	8.17	6.99	11	12.6
	URPD	12.3	11.8	5.36	3.76	7.73	7.67
Corrected with CCNY algorithm	R^2	0.749	0.878	0.961	0.957	0.906	0.972
	ARPD	17.8	13.3	6.09	5.04	8.76	10.2
	URPD	9.65	9.41	3.46	2.11	5.28	5.59

First row: Before the bidirectional effect is removed (the 60° ≤ φ ≤ 180° range is given first, and the 80° ≤ φ ≤ 100° range is shown in parentheses). Second row: After the bidirectional effect is corrected with the MG algorithm. Third row: Corrected with the CCNY algorithm.

Table 4. AAPD Values from the Comparison between the $Rrs_{MODIS}^0(\lambda)$ and $Rrs_{Spr}^0(\lambda)$ Data

AAPD (%)	Wavelength (nm)				
	412	443	491	551	668
MG	46.43	38.85	16.68	13.61	24.54
CCNY	42.40	34.16	14.93	10.99	21.89
Improvement	4.03	4.69	1.75	2.62	2.65

for the comparisons processed with the CCNY algorithm. The dispersion between the satellite and *in situ* data, especially for high $Rrs^0(\lambda)$ values (which are usually associated with high particulate loading in the water), is reduced for the CCNY processing, thereby exhibiting its appropriateness for use in the bidirectional correction for coastal water types.

7. Summary and Conclusion

We first created a dataset of remote sensing reflectance spectra, $Rrs(\theta_v, \theta_s, \phi, \lambda)$, through radiative transfer simulations made with Hydrolight. Simulations were performed for all ranges of viewing and illumination geometries, with input parameters of the IOP model generated as uniformly distributed random variables in the prescribed ranges typical for coastal waters. Then, $Rrs(\lambda)$ values simulated for all viewing and illumination geometries were parameterized with the single backscattering albedo, $\omega(\lambda)$, for each set of geometries. Based on this parameterization, we proposed an LSQ fit third order polynomial remote sensing reflectance model as a function of the backscattering albedo, for which coefficients were tabulated as a lookup table for the sets of illumination and viewing geometries and wavelengths to estimate the directional variation of the water-leaving radiance field of typical case 2 water conditions.

We then carried out the assessments of the bidirectional correction performed with the CCNY model as well as the operational MG algorithm based on the simulated dataset. Our assessments showed that the proposed CCNY algorithm demonstrates advantages over the operational MG algorithm. The retrieval errors resulting from CCNY BRDF corrections are relatively small and have AAPD values in the range of 0.42%–0.85%. These small retrieval errors mostly come from the LSQ fitting procedure and are well below the well-known bidirectional variation of 10%–20%. In addition, the regression lines between the retrieved and the actual remote sensing reflectance are very close to the 1:1 line for all viewing and illumination geometries. On the other hand, comparisons carried out using the current MG algorithm depict high AAPD values in the range of 6.2%–9.54%. In addition, more than 57% of the MG retrievals are outside the range of 5% accuracy targeted by the OC sensor validation procedure. Systematic variations of the slope and of the bias with the scattering angles are also observed at all wavelengths for the comparisons. These results indicate

that the MG algorithm, which is optimized for the case 1 water condition, with [Chl] being the main input, is unsuited for use in optically complex case 2 waters if the OC sensor validation procedure's 5% retrieval accuracy target is to be achieved.

We also carried out comparisons of two algorithms for the above-water radiometric dataset of LISCO, which offers the unique capability of making near-concurrent water-leaving radiance measurements from different viewing geometries. LISCO's instrumentation setup, in which two instruments acquire the data almost concurrently but at different scattering angles with respect to the Sun, is the major advantage we have with regard to analyzing the fidelity of bidirectional correction algorithms: we can compare the final remote sensing products, Rrs^0 , retrieved from the measurements made by two instruments acquiring data at different viewing geometries. Comparisons are performed at all SeaPRISM wavelengths. With the proposed algorithm, comparison between the final remote sensing reflectance product of HyperSAS denoted as Rrs_{HS}^0 and that of SeaPRISM denoted as Rrs_{Spr}^0 exhibits a spectral average AAPD value of 10.2% and very a strong correlation, with an R^2 value of 0.972. On the other hand, the spectral average AAPD value of the comparison with the data processed with the current MG algorithm is 12.6%, and the R^2 value is 0.958.

Finally, we tested merits of the proposed CCNY BRDF algorithm over the current operational MG algorithm by comparing MODIS data with *in situ* data. The study clearly shows that comparisons between MODIS and *in situ* data that are processed with the CCNY algorithm exhibit smaller AAPD values throughout the spectrum, with a spectral average improvement of 3.15%. In addition, stronger correlation coefficients were also observed in the comparison carried out with $Rrs^0(\lambda)$ data processed with the CCNY algorithm.

In conclusion, we propose a remote sensing reflectance model specifically tuned with coastal water IOPs for bidirectional correction. The resulting algorithm shows advantages over the current MG algorithm on the tests performed with simulated datasets, *in situ* measured data sets (for a one-year period), and satellite data. We propose the use of this CCNY BRDF correction algorithm for better ocean color data retrievals as well as validation and calibration for coastal waters.

This work has been partially supported by grants from NOAA and the Office of Naval Research. We would like to thank the NASA AERONET team for SeaPRISM calibration, data processing, and support of site operations and the NASA Ocean Color Processing Group for satellite imagery. We would also like to thank T. Legbandt and I. Ioannou for help in operating LISCO instruments and useful discussions. We are grateful to the editor and two anonymous reviewers for their comments and useful suggestions.

References

1. A. Morel and B. Gentili, "Diffuse reflectance of oceanic waters. II. bidirectional aspects," *Appl. Opt.* **32**, 6864–6872 (1993).
2. A. Morel, K. J. Voss, and B. Gentili, "Bidirectional reflectance of oceanic waters: a comparison of modeled and measured upward radiance fields," *J. Geophys. Res.* **100**, 13143–13150 (1995).
3. C. K. Gatebe, M. D. King, A. I. Lyapustin, G. T. Arnold, and J. Redemann, "Airborne spectral measurements of ocean directional reflectance," *J. Atmos. Sci.* **62**, 1072–1092 (2005).
4. K. J. Voss and A. Morel, "Bidirectional reflectance function for oceanic waters with varying chlorophyll concentrations: measurements versus predictions," *Limnol. Oceanogr.* **50**, 698–705 (2005).
5. A. Morel, D. Antoine, and B. Gentili, "Bidirectional reflectance of oceanic waters: accounting for Raman emission and varying particle scattering phase function," *Appl. Opt.* **41**, 6289–6306 (2002).
6. Y.-J. Park and K. Ruddick, "Model of remote-sensing reflectance including bidirectional effects for case 1 and case 2 waters," *Appl. Opt.* **44**, 1236–1249 (2005).
7. A. Gilerson, J. Zhou, R. Fortich, I. Ioannou, S. Hlaing, B. Gross, F. Moshary, and S. Ahmed, "Spectral dependence of the bidirectional reflectance function in coastal waters and its impact on retrieval algorithms," in *Proceedings of IEEE International Geoscience and Remote Sensing Symposium, 2007 (IEEE, 2007)*, pp. 3777–3780.
8. Z. Lee, K. L. Carder, C. D. Mobley, R. G. Steward, and J. S. Patch, "Hyperspectral remote sensing for shallow waters. I. a semianalytical model," *Appl. Opt.* **37**, 6329–6338 (1998).
9. Z. Lee, K. L. Carder, C. D. Mobley, R. G. Steward, and J. S. Patch, "Hyperspectral remote sensing for shallow waters. 2. deriving bottom depths and water properties by optimization," *Appl. Opt.* **38**, 3831–3843 (1999).
10. A. Albert and C. Mobley, "An analytical model for subsurface irradiance and remote sensing reflectance in deep and shallow case-2 waters," *Opt. Express* **11**, 2873–2890 (2003).
11. A. Albert and P. Gege, "Inversion of irradiance and remote sensing reflectance in shallow water between 400 and 800 nm for calculations of water and bottom properties," *Appl. Opt.* **45**, 2331–2343 (2006).
12. Z. P. Lee, K. Du, K. J. Voss, G. Zibordi, B. Lubac, R. Arnone, and A. Weidemann, "An inherent-optical-property-centered approach to correct the angular effects in water-leaving radiance," *Appl. Opt.* **50**, 3155–3167 (2011).
13. S. Ahmed, T. Harmel, R. A. Arnone, A. Gilerson, S. Hlaing, and A. D. Weidemann, "Multi- and hyperspectral ocean color measurements from Long Island Sound observation platform (LISCO): comparison with satellite measurements & assessments of uncertainties," presented at Ocean Optics XX, Anchorage, Alaska, United States, 27–30 September 2010.
14. S. Hlaing, T. Harmel, A. Ibrahim, I. Ioannou, A. Tonizzo, A. Gilerson, and S. Ahmed, "Validation of ocean color satellite sensors using coastal observational platform in Long Island Sound," *Proc. SPIE* **7825**, 782504 (2010).
15. T. Harmel, A. Gilerson, S. Hlaing, A. Tonizzo, T. Legbandt, A. Weidemann, R. Arnone, and S. Ahmed, "Long Island Sound Coastal Observatory: assessment of above-water radiometric measurement uncertainties using collocated multi and hyperspectral systems," *Appl. Opt.* **50**, 5842–5860 (2011).
16. C. D. Mobley, "Estimation of the remote-sensing reflectance from above-surface measurements," *Appl. Opt.* **38**, 7442–7455 (1999).
17. H. R. Gordon, J. W. Brown, R. H. Evans, O. B. Brown, R. C. Smith, K. S. Baker, and D. K. Clark, "A semianalytic radiance model of ocean color," *J. Geophys. Res.* **93**, 10909–10924 (1988).
18. P. Gege and A. Albert, "A tool for inverse modeling of spectral measurements in deep and shallow waters," in *Remote Sensing of Aquatic Coastal Ecosystem Processes: Science and Management Applications*, L. L. Richardson and E. F. LeDrew, eds. (Springer, 2006), pp. 81–109.
19. Z. P. Lee, K. L. Carder, and R. A. Arnone, "Deriving inherent optical properties from water color: a multiband quasi-analytical algorithm for optically deep waters," *Appl. Opt.* **41**, 5755–5772 (2002).
20. A. Morel and B. Gentili, "Diffuse reflectance of oceanic waters. III. implication of bidirectionality for the remote-sensing problem," *Appl. Opt.* **35**, 4850–4862 (1996).
21. H. R. Gordon, "Normalized water-leaving radiance: revisiting the influence of surface roughness," *Appl. Opt.* **44**, 241–248 (2005).
22. C. D. Mobley and L. K. Sundman, *HYDROLIGHT 5 ECO-LIGHT 5 Users' Guide* (Sequoia Scientific, Inc., 2008).
23. R. M. Pope and E. S. Fry, "Absorption spectrum (380–700 nm) of pure water. II. integrating cavity measurements," *Appl. Opt.* **36**, 8710–8723 (1997).
24. C. Mobley and L. Sundman, *HYDROLIGHT 4.2* (Sequoia Scientific, Inc., 2001).
25. A. M. Ciotti, M. R. Lewis, and J. J. Cullen, "Assessment of the relationships between dominant cell size in natural phytoplankton communities and the spectral shape of the absorption coefficient," *Limnol. Oceanogr.* **47**, 404–417 (2002).
26. A. A. Gilerson, A. A. Gitelson, J. Zhou, D. Gurlin, W. Moses, I. Ioannou, and S. A. Ahmed, "Algorithms for remote estimation of chlorophyll-a in coastal and inland waters using red and near infrared bands," *Opt. Express* **18**, 24109–24125 (2010).
27. D. Stramski, A. Bricaud, and A. Morel, "Modeling the inherent optical properties of the ocean based on the detailed composition of the planktonic community," *Appl. Opt.* **40**, 2929–2945 (2001).
28. A. Bricaud, M. Babin, A. Morel, and H. Claustre, "Variability in the chlorophyll-specific absorption coefficients of natural phytoplankton: analysis and parameterization," *J. Geophys. Res.* **100**, 13321–13332 (1995).
29. M. S. Twardowski, E. Boss, J. B. Macdonald, W. S. Pegau, A. H. Barnard, and J. R. V. Zaneveld, "A model for estimating bulk refractive index from the optical backscattering ratio and the implications for understanding particle composition in case I and case II waters," *J. Geophys. Res.* **106**, 14129–14142 (2001).
30. K. Voss, "A spectral model of the beam attenuation coefficient in the ocean and coastal areas," *Limnol. Oceanogr.* **37**, 501–509 (1992).
31. A. Morel, "Optical properties of pure water and pure seawater," in *Optical Aspects of Oceanography*, N. G. Jerlov and E. S. Nielsen, eds. (Academic, 1974), pp. 1–24.
32. C. D. Mobley, *Light and Water: Radiative Transfer in Natural Waters* (Academic, 1994).
33. T. J. Petzold, "Volume scattering functions for selected ocean waters," DTIC Document (DTIC, 1972).
34. C. D. Mobley, L. K. Sundman, and E. Boss, "Phase function effects on oceanic light fields," *Appl. Opt.* **41**, 1035–1050 (2002).
35. G. Fournier and J. L. Forand, "Analytic phase function for ocean water," *Proc. SPIE* **2258**, 194–201 (1994).
36. Z.-P. Lee, ed., "Remote sensing of inherent optical properties: fundamentals, tests of algorithms, and applications," Reports of the International Ocean-Colour Coordinating Group, **No. 5** (IOCCG, 2006).
37. A. Gilerson, J. Zhou, S. Hlaing, I. Ioannou, J. Schalles, B. Gross, F. Moshary, and S. Ahmed, "Fluorescence component in the reflectance spectra from coastal waters. dependence on water composition," *Opt. Express* **15**, 15702–15721 (2007).
38. A. W. Harrison and C. A. Coombes, "An opaque cloud cover model of sky short wavelength radiance," *Sol. Energy* **41**, 387–392 (1988).
39. W. W. Gregg and K. L. Carder, "A simple spectral solar irradiance model for cloudless maritime atmospheres," *Limnol. Oceanogr.* **35**, 1657–1675 (1990).
40. G. Zibordi, J. F. Berthon, F. Mélin, D. D'Alimonte, and S. Kaitala, "Validation of satellite ocean color primary products at optically complex coastal sites: northern Adriatic Sea, northern Baltic Proper and Gulf of Finland," *Remote Sens. Environ.* **113**, 2574–2591 (2009).
41. G. Zibordi, F. Mélin, S. B. Hooker, D. D'Alimonte, and B. Holben, "An autonomous above-water system for the validation of ocean color radiance data," *IEEE Trans. Geosci. Remote Sens.* **42**, 401–415 (2004).

42. S. B. Hooker, G. Zibordi, J. F. Berthon, and J. W. Brown, "Above-water radiometry in shallow coastal waters," *Appl. Opt.* **43**, 4254–4268 (2004).
43. J. E. O'Reilly, S. Maritorena, B. G. Mitchell, D. A. Siegel, K. L. Carder, S. A. Garver, M. Kahru, and C. McClain, "Ocean color chlorophyll algorithms for SeaWiFS," *J. Geophys. Res.* **103**, 24937–24953 (1998).
44. H. J. Gons, M. Rijkeboer, and K. G. Ruddick, "A chlorophyll-retrieval algorithm for satellite imagery (medium resolution imaging spectrometer) of inland and coastal waters," *J. Plankton Res.* **24**, 947–951 (2002).
45. D. McKee, A. Cunningham, D. Wright, and L. Hay, "Potential impacts of nonalgal materials on water-leaving Sun induced chlorophyll fluorescence signals in coastal waters," *Appl. Opt.* **46**, 7720–7729 (2007).
46. G. Zibordi, B. N. Holben, I. Slutsker, D. Giles, D. D'Alimonte, F. Mélin, J. F. Berthon, D. Vandemark, H. Feng, and G. Schuster, "AERONET-OC: a network for the validation of ocean color primary radiometric products," *J. Atmos. Ocean. Technol.* **26**, 1634–1651 (2009).
47. <http://aeronet.gsfc.nasa.gov>.
48. S. Kay, J. D. Hedley, and S. Lavender, "Sun glint correction of high and low spatial resolution images of aquatic scenes: a review of methods for visible and near-infrared wavelengths," *Remote Sens.* **1**, 697–730 (2009).
49. <http://oceancolor.gsfc.nasa.gov>.